Synthesis and crystal structures of two polymorphs of $Li_{4-2x}Mg_{1+x}TeO_6$

Authors: Alex J. Brown[1], Jiatu Liu[1], Frederick P. Marlton[1], Maxim Avdeev[1,2], Brendan J. Kennedy[1], Chris D. Ling[1]

1. School of Chemistry, The University of Sydney, Sydney 2006, Australia
2. Australian Centre for Neutron Scattering, ANSTO, Kirrawee 2232, Australia

Abstract

Two polymorphs of lithium magnesium tellurate $Li_{4-2x}Mg_{1+x}TeO_6$ have been prepared by solid-state reactions and their crystal structures characterised by powder X-ray and neutron diffraction. For $x \approx 0$, a monoclinic $C2/m$ phase is obtained, structurally similar to other O3 type honeycomb layered tellurate and antimonate compounds. The basic structure consists of $[Mg_2TeO_6]^{3-}$ honeycomb layers alternating with Li layers, with some anti-site disorder of Li and Mg between layers, analogous to the structure of Li_4ZnTeO_6. For $0 < x < {\sim}0.5$ (specifically, $x = 0.33$) an orthorhombic $Fddd$ phase is obtained, with a rock-salt superstructure containing disordered Li/Mg cation sites surrounding ordered TeO_6 octahedra, analogous to the structure of $Li_3Co_2TaO_6$.

Introduction

Layered mixed-metal oxides in which two metals are separated by alkali-metal cations (Li^+, Na^+ and K^+) are an area of functional inorganic materials research due to the stability of the oxides and the range of synthetic routes available. An important class of layered mixed-metal oxides is the ordered superstructures possessing the general formula $A_xM_2M'O_6$ which form "honeycomb" structures. These honeycomb structures have $M'O_6$ octahedra surrounded by six edge-sharing MO_6 octahedra, which form brucite-type MO_2 sheets, with A^+ intercalating

between the MO_2 sheets. A broad range of compositions have been shown to form honeycomb-type phases, including $A_3M_2M'O_6$ (A = Li$^+$, Na$^+$; M = Mg, Co, Ni, Cu, Zn; M' = Sb, Bi), $A_2M_2TeO_6$ (A = Li$^+$, Na$^+$, K$^+$; M = Mg, Co, Ni, Cu, Zn) and Li$_4MTeO_6$ (M = Co, Ni, Cu, Zn).[1–24]

A focus of research on these honeycomb oxides has been their ionic conductivity, both as solid-state electrolytes and as cathodes for Li-ion and Na-ion batteries. For example, the family of fast sodium ion conductors Na$_2M_2TeO_6$ (M = Ni, Co, Zn, Mg), first characterised by Evstigneeva et $al.$, show promise as electrolytes in all solid-state batteries.[18] The sodium tellurates have trigonal prismatic "P2-type" coordination of the Na cations and depending on the metal cation M different stacking sequences are observed. [18] Na$_2$Ni$_2$TeO$_6$ crystallises in the hexagonal $P6_3/mcm$ space group and has all the Ni and Te atoms aligned along the c-axis between cationic layers. While M = Mg, Zn, Co crystallises in the $P6_3$22 space group and has alternating layers of M and Te along the c-axis. The Na$_2M_2TeO_6$ (M = Zn, Mg) compounds have high reported ionic conductivities between 10^{-4} and 10^{-3} S cm^{-1}.[24–26] This high conductivity may be due to the 2D conduction pathways and low activation energy of the Na cations within the alkali metal layer.

As cathode materials, the Te-based honeycomb oxides tend to show higher reversible capacities, at high voltages compared to the other possible high-valence cations Sb or Bi. For example, Na$_2$Ni$_2$TeO$_6$ has been found to have reversible capacity of at least 100 mAh g^{-1} over the range 3-4.3 V.[21] The Li tellurate Li$_4$NiTeO$_6$ reversibly reacts with Li$^+$/Li^0 at a potential of 4.2 V due to the Ni^{4+}/Ni^{2+} redox, with a capacity of about 110 mAhg^{-1}.[22] The recently reported family of potassium tellurates, K$_2M_2TeO_6$ (M = Ni, Mg, Zn, Co and Cu) show reversible K-ion insertion with good ionic conductivity of 0.01 mS cm^{-1} at room temperature.[23]

Another area of interest of the honeycomb oxides has been their low-temperature magnetism. Paramagnetic cations arranged on the honeycomb topology can give rise to frustrated magnetism, including the "zig-zag" antiferromagnetic (AFM) magnetic ground-state, which breaks hexagonal symmetry, and spin-glass behaviour for some of the Cu containing compounds.[7,10,12,27–29] We recently showed, concurrently with and independently of Stratan et $al.,$ that Li$_3$Co$_2$SbO$_6$ is the first honeycomb oxide known to have an A-type AFM groundstate.[14,15] Li$_3$Co$_2$SbO$_6$ also displays metamagnetism, with the A-type AFM groundstate

undergoing a spin-flop transition to ferromagnetism under a sufficient applied magnetic field.[15]

Of the Li_4MTeO_6 type compounds, the compositions with M^{2+} = Co, Ni, Cu, Zn have been described with lattice parameters and limited structural data reported.[16,19] These compounds can be rewritten as $Li_3(Li,M)TeO_6$ where most of the Li occupies the octahedral O3-type alkali metal layer with the remainder occurring in mixed Li/M sites in the alternate octahedral intercalation layers. Li_4MgTeO_6 is a composition which is plausible within the Li_4MTeO_6 family of honeycomb structures. The composition was first suggested by Nalbandyan *et al.* but has not yet been reported in the literature.[19] To address this absence the synthesis and structural characterisation of two polymorphs of Li_4MgTeO_6 are reported for the first time in this work.

Experimental

Samples were synthesised targeting the nominal composition Li_4MgTeO_6. The reagents Li_2CO_3 (99%, Merck), MgO (98%, Merck) and TeO_2 (99.9%, Sigma-Aldrich) were mixed thoroughly in a mortar and pestle. The powders were then pressed into pellets and placed in alumina crucibles. The samples were first heated to 600 °C, at a rate of 8 °C /min for a couple of hours to expel CO_2 followed by a higher temperature calcine at 850 °C for 12 hours. After heating the samples were left in the furnace until cooled to room temperature. Multiple reheating steps at 850 °C with intermittent regrinding followed until the samples equilibrated and minimal impurities were identified in XRD patterns. Polycrystalline samples were characterised using a PANalytical X'Pert Pro Diffractometer which operates in a Bragg-Brentano θ-2θ geometry. A copper X-ray tube operating with a voltage of 45 kV and 40 mA was used to generate Cu K_α radiation ($K_{\alpha1}$, λ = 1.5406 Å; $K_{\alpha2}$, λ = 1.5444 Å). A nickel filter was used to remove Cu K_β radiation. Polycrystalline samples were finely ground and flattened in stainless steel sample holders, with a zero-background Si plate. Data were collected using a scanning rate of 0.045 2θ/s, over a range 5° < 2θ < 120° using a PIXcel 1D detector. For Rietveld refinement TOPAS version 5 was used.[30] Room-temperature NPD data were collected on ECHINDA, the high-resolution powder diffractometer at the OPAL research reactor, ANSTO, Australia.[31,32] Constant wavelengths of λ = 1.6215 Å and 2.4395 Å and the data were measured between 5° and 165° 2θ. Ionic conductivity measurements were performed using electrochemical impedance spectroscopy (EIS), from a BioLogic MTZ

Impedance Spectrometer with a Biologic furnace attachment. Samples were sintered before being run from (0.1 Hz to – 10 MHz, 0.2 V) room temperature to 200 °C, at 20 °C increments. These measurements are not included in the results due to the very low ionic conductivities observed.

Results and Discussion

XRD data for the first sample of Li_4MgTeO_6, synthesised at its nominal composition, is shown in Figure 1. Note that this figure includes a Rietveld fit to the structural model subsequently obtained by refinement against NPD data (see below and Figure 2). All peaks could be indexed to a monoclinic unit cell with $C2/m$ symmetry, analogous to the Li_4ZnTeO_6 structure.[19] In the diffraction pattern there is a slight anisotropic peak broadening moving to higher angles. This slight peak broadening could be caused by ordering within the cationic layers but relative disorder of the cations between layers.
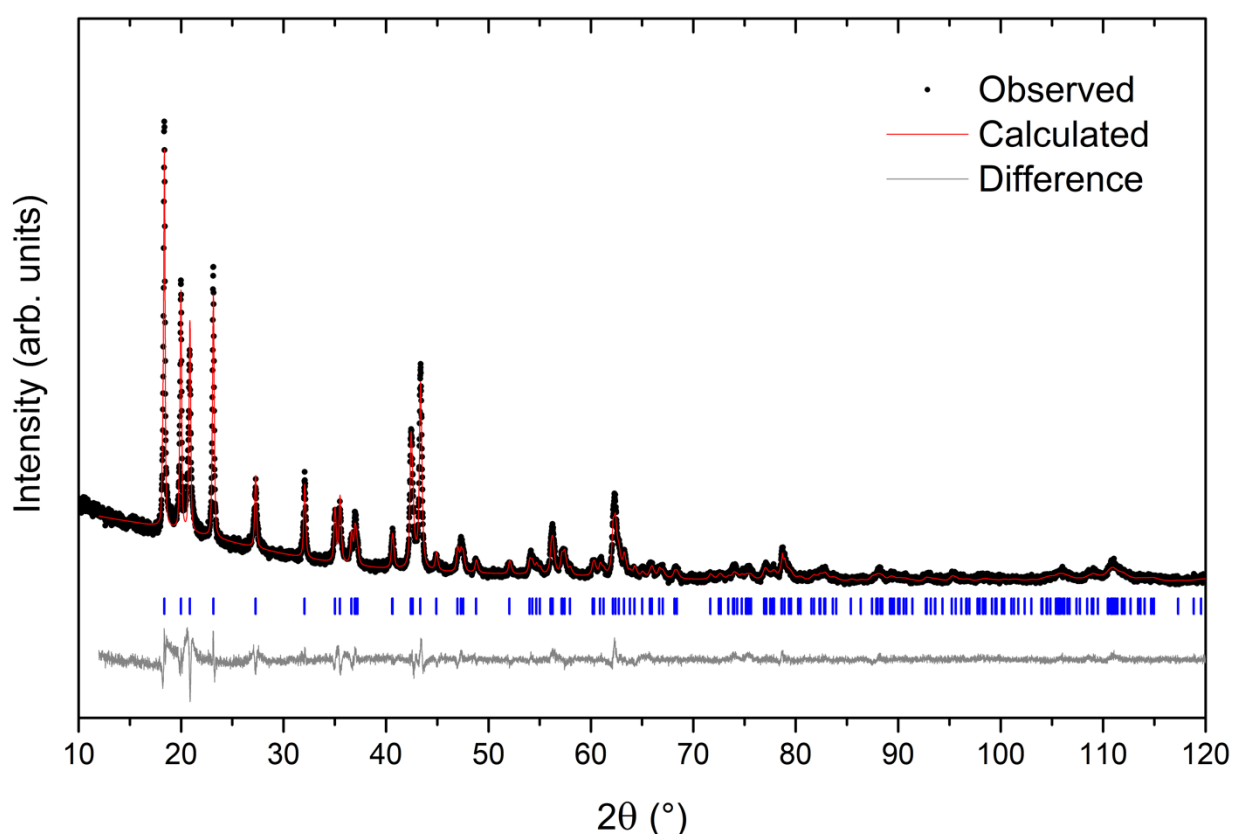

Figure 1 *Powder XRD data (Cu $K_α$, λ = 1.5418 Å) for the first sample of Li_4MgTeO_6 at room temperature. Note that the Rietveld fit shown is to the structural model subsequently obtained*

The sloping background observed in XRD at low angles out to ~30° 2θ is qualitatively indicative of stacking faults, a common feature of honeycomb oxides.[19,33,34] In an ideal layered mixed-metal oxide, all the cationic planes are stacked along the c-axis by a unique translational stacking vector.[35] However it has been shown that two other stacking vectors with very similar energy (1-2 meV) can occur in a structure, leading to so called "stacking faults".[36] Stacking faults in the honeycomb oxides occur due to the relatively weak coupling between the MO$_2$ layers separated by the alkali cations. In practice, the cationic layers are never perfectly stacked along the c-axis when a layered structure has the $C2/m$ space group, although higher temperature thermal treatment during synthesis can decrease the frequency of stacking faults.[35]

Rietveld refinement of monoclinic Li$_4$MgTeO$_6$ against XRD data for structural determination proved difficult. Due to a combination of preferred orientation of the plate-like crystallites in flat-plate geometry, and the insensitivity of X-rays to light Li atoms. NPD data (collected using large sample cans) overcomes both problems and was therefore used for the final full structure refinement.

The final Rietveld fit of monoclinic Li$_4$MgTeO$_6$ to NPD data is shown in Figure 2. The structure is similar to other reported members of the Li$_4$$MTeO_6$ family of compounds (M = Zn, Co, Ni, Cu). These Li$_4$$MTeO_6$ phases show cation ordering approximated by the prototypical Li$_3$Zn$_2$SbO$_6$ type layered honeycomb oxides, but usually with the addition of considerable stacking disorder. In these phases the TeO$_6$ octahedra maximise their distances within the metal layer; however, the surrounding MO$_6$ sites show anti-site mixing of M and Li. We tested for Li/Mg partial occupancy on the Te sites in Rietveld refinements against both NPD and XRD data. In both cases, the Te occupancy refined to 1 within error, and was therefore fixed as such.

Note that a small (~2%) MgO impurity included in the Rietveld refinement (Figure 2) suggests some slight Li evaporation during the heat treatment. We therefore repeated the synthesis with excess Li$_2$CO$_3$ (5-10% by weight), and the MgO impurity was indeed eliminated; however, a more prominent Li$_4$TeO$_5$ impurity (>10%) was obtained instead. The small unit cell and simple composition of MgO make it easier to account for in Rietveld

refinements, therefore, the stoichiometric synthesis was preferred. It appears that Li is lost more readily from the target compound than from Li_4TeO_5, making a completely impurity-free sample elusive.

The crystal structure of monoclinic Li_4MgTeO_6 is illustrated in Figure 2 and Table 1 gives the refined structural parameters. The final refined unit cell dimensions are a = 5.185(5) Å, b = 8.874(9) Å, c = 5.161(6) Å, and β = 110.73(6)°. The average interatomic distances in the octahedra are summarised in Table 2.

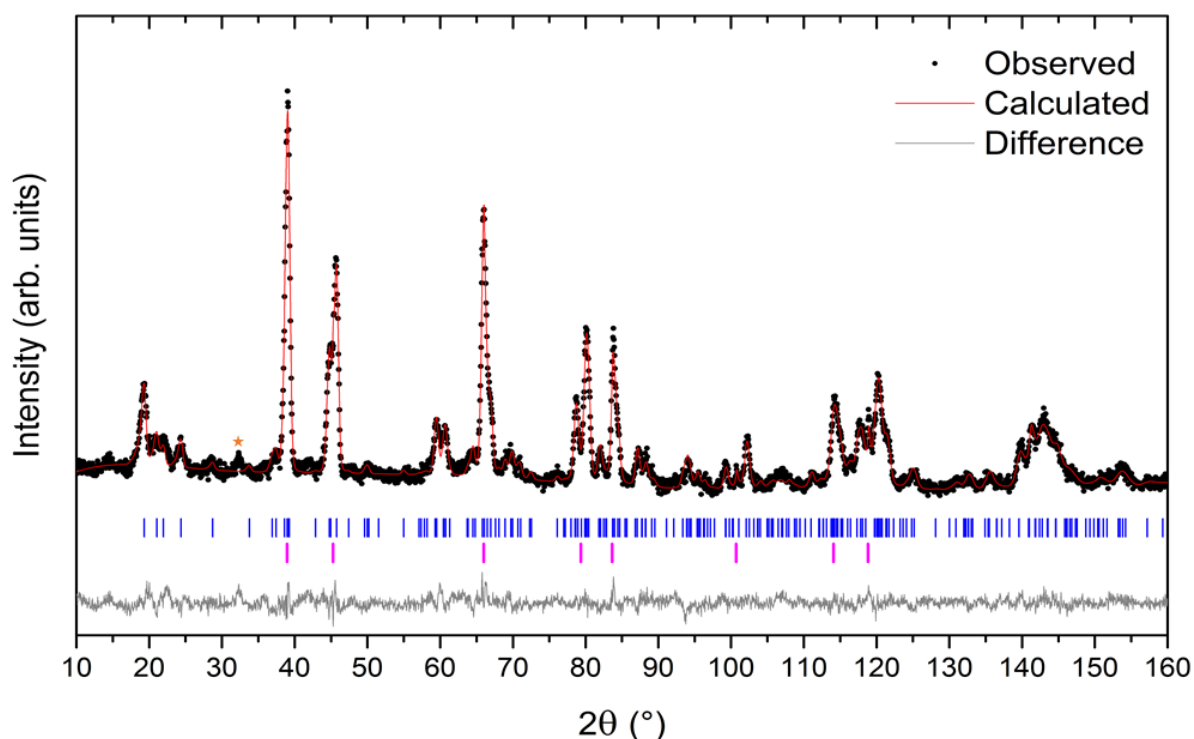***Figure 2*** *Rietveld fit of monoclinic Li_4MgTeO_6 to NPD (λ = 1.6215 Å) data at room temperature. Observed data are black circles, calculated fit is red and the difference curve is grey. Blue tick marks show Bragg reflections for Li_4MgTeO_6 and pink tick marks for the minor MgO (~2%) impurity. The orange star identifies an impurity peak which could not be indexed.*

Table 1 Unit cell dimensions, fractional atomic coordinates, site occupancies, and isotropic atomic displacement parameters B_{iso} for monoclinic Li_4MgTeO_6, from Rietveld refinement against NPD data at room temperature.

C2/m Li$_4$MgTeO$_6$		Crystal system Monoclinic		Space Group C2/m	
GOF = 1.32, R$_{wp}$ = 4.41%					
Radiation	a (Å)	b (Å)	c (Å)	β (deg)	Volume (Å^3)
NPD (λ = 1.6215)	5.1849(6)	8.8749(8)	5.1619(6)	110.75(6)	222.11(4)
Cu Kα XRD	5.1849(3)	8.8804(5)	5.1612(4)	110.76(3)	222.21(3)

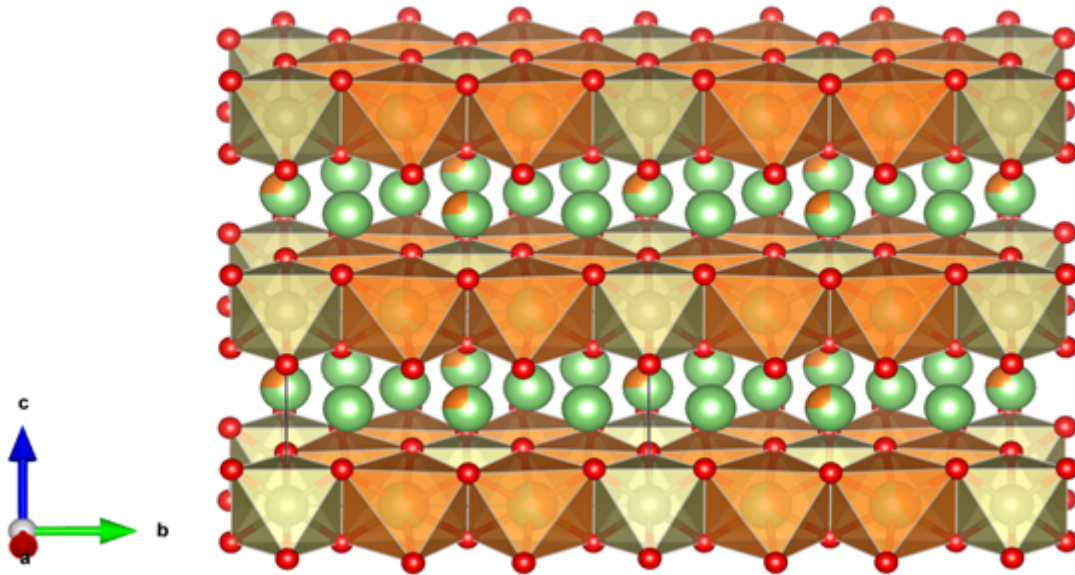| Atom	x	y	z	Occ.	B$_{iso}$	Wyckoff Site
Te^{6+}	0	0	0	1	1.13(11)	2a
Li$^+$(1)	0	0.170(2)	1/2	1	1.5(4)	4h
Mg^{+2}(1)	0	0.322(4)	0	0.379(6)	0.4(3)	4g
Li$^+$(2)	0	0.322(4)	0	0.621(6)	0.4(3)	4h
Mg^{2+}(2)	0	1/2	1/2	0.241(1)	1.0(1)	2d
Li$^+$(3)	0	1/2	1/2	0.759(1)	1.0(1)	2d
O1	0.7716(6)	0	0.2235(3)	1	0.38(13)	4i
O2	0.2312(5)	0.152(5)	0.2365(7)	1	0.17(6)	8j

Figure 3: *Crystal structure of monoclinic (C2/m) O3-type honeycomb Li$_4$MgTeO$_6$. (Mg,Li)O$_6$ octahedra are orange, TeO$_6$ octahedra are ivory, O atoms are red and Li atoms are green. One of the sites in the alkali metal layer has mixed occupancy of both Mg^{2+} and Li$^+$, as indicated by the green/orange wedges.*

Table 2: Selected interatomic distances (Å) for monoclinic Li_4MgTeO_6 at room temperature

Te–O1(x2)	1.923(2)	(Li3,Mg2)–O1 (x2)	2.333(6)
Te–O2 (x4)	1.926(2)	(Li3,Mg2)–O2 (x4)	2.066(5)
Average	1.925	Average	2.15
Sum of Radii	1.96	Sum of Radii	2.15
BVS (Te^{6+})	5.87	BVS (Li^+, Mg^{2+})	1.04, 1.91
Li1–O1 (x2)	2.126(2)	(Li2,Mg1)–O1 (x2)	2.158(3)
Li1–O2 (x2)	2.113(1)	(Li2,Mg1)–O2 (x2)	2.041(2)
Li1–O2 (x2)	2.223(1)	(Li2,Mg1)–O2 (x2)	2.166(5)
Average	2.154	Average	2.121
Sum of Radii	2.16	Sum of Radii	2.14
BVS (Li^+)	0.94	BVS (Li^+, Mg^{2+})	0.98, 1.81

The site occupancy of the MO_6 $4g$ Wyckoff symmetry site was refined allowing for mixed occupancy of Li and Mg, as for Li_4ZnTeO_6.[19] The large difference in neutron scattering lengths between Li (-1.90 fm) and Mg (5.375 fm) affords sensitivity to the distribution of these two cations. The sum of the occupancies of Li and Mg were constrained to be 1, and the Mg^{2+} : Li^+ ratio was found to be 0.379(6) : 0.621(6). As noted by earlier authors,[19] ordering of Li^+ and Mg^{2+} on the intercalation sites would be incompatible with the mirror plane, giving instead the space group $C2$. Based on the refinement we find no evidence for Li/Mg ordering. However, in principle it is possible that each individual layer is ordered (as in the $C2$ model) for the Li_4MTeO_6 compounds but stacking disorder results in the observed $C2/m$ designation.[37] The possibility of Li-Mg mixing in the alkali metal layer was introduced to the model by constraining the occupancies on the $4h$ and $2d$ sites in a similar manner. For the $4h$ site, no evidence of mixing was found, with the occupancy of Li^+ converging to 1 within error. The $2d$ site refined to a Mg^{2+}: Li^+ ratio of 0.241(1):0.759(1) This mixing is slightly larger than that found for Li/Zn at the $2d$ site in Li_4ZnTeO_6, which contained 13.1% Zn^{2+}.[19] Li (0.76 Å) and Mg (0.72 Å) have similar ionic radii, so they can substitute for each other in their respective sites without significant spatial penalty.[38] Therefore, it is not surprising to find a minor amount of Mg inclusion into the alkali metal layer. The refined compositional formula $Li_{4.001}Mg_{0.999}TeO_6$ is in excellent agreement with the nominal formula.

Orthorhombic Li$_{3.34}$Mg$_{1.33}$TeO$_6$

While trying to optimise the purity of the monoclinic phase of Li$_4$MgTeO$_6$ by manipulating the Li:Mg ratio, we prepared solid-solution phases Li$_{4-2x}$Mg$_{1+x}$TeO$_6$ with nominal compositions x = 0, 0.25, 0.50, 1.00, 1.50. The progression of XRD patterns across the solid-solution is presented as Supplementary Information (Figure S1). For x = 0, the monoclinic phase of Li$_4$MgTeO$_6$ dominates, but for x = 0.25 and 0.50, a structurally distinct rock-salt superstructure phase appears. XRD analysis showed the new phase to be isostructural with the recently reported orthorhombic *Fddd* phase of Li$_3$Co$_2$SbO$_6$.[15] However, increasing the Mg:Li ratio further to x = 1.00, corresponding to a hypothetical analogue Li$_2$Mg$_2$TeO$_6$ (note the reduced Li content in line with the increased charge on Te^{6+} vs. Sb^{5+}), failed. For x > 0.5, Mg$_3$TeO$_6$ [39] was the dominant phase, with the excess Li presumably evaporating during synthesis, or forming Li$_2$O which converts to poorly crystalline Li$_2$CO$_3$ on exposure to air.

The structure was Rietveld-refined against XRD data using an initial model derived from that of Li$_3$Co$_2$SbO$_6$,[15] and including fractional occupancy and inter-site disorder schemes analogous to other known *Fddd* orthorhombic rock-salt structures including Li$_3$Mg$_2$NbO$_6$, Li$_3$Co$_{1.06(1)}$TeO$_6$ and Li$_3$Co$_2$SbO$_6$.[15,41,42] Initially, additional Mg occupancy was only refined on the Li(1) 16g site, with Li and Mg constrained to add up to full occupancy. The best fit (R$_{wp}$ = 9.60%, GOF = 2.09) gave a Li:Mg ratio of 0.51859:0.48141. We then similarly allowed partial Mg occupancy on the Li(3) 16g site, which refined to zero within error and was fixed as such; and the Li(2) 8b site. The best fit (R$_{wp}$ = 9.17%, GOF = 1.99) had Li:Mg ratios on the 16g Li(1) site of 0.485(16): 0.515(16)and on the 8b Li(2) site of 0.674(16): 0.326(16), giving an overall composition Li$_{3.644}$Mg$_{1.356}$TeO$_6$. However, this composition is not chemically plausible, assuming full oxygen occupancy and all Te in the 6+ oxidation state.

The excess cationic charge can be eliminated by assuming the existence of Li vacancies throughout the lattice. Vacancies were introduced onto the Li(3) site changing the Li site occupancy from 1.0 to 0.837. Furthermore, as the refined Mg:Li occupancy on the Li(1) site was found to be within error of 0.5, it was constrained as such in the final refinement cycles. This resulted in a final refinement with statistics of: R$_{wp}$ = 9.20%, GOF = 2.00, and a chemical composition of Li$_{3.34}$Mg$_{1.33}$TeO$_6$. Interatomic distances for the rock-salt polymorph from the final refinement are given in Table 4. Average bond lengths relative to effective

ionic radii data, and bond valence sums (BVS), are consistent with expectations for the respective ions.

As for our sample of monoclinic $C2/m$ Li_4MgTeO_6, an unindexed peak is observed at ~34° 2θ in the XRD pattern. The position of this peak is consistent with, although not definitive proof of, poorly crystalline Li_2CO_3. Some Li_4TeO_5 (~4% weight fraction) is also present in the sample. Additionally, an unindexed peak from a secondary occurred at ~19.8° 2θ, which slightly overlapped with the next peak from the main phase. This peak was difficult to index meaningfully, and hence it was fit with a single symmetrical Gaussian peak. This prevented the main phase from unphysically fitting the increased intensity in the overlapped region.

The final Rietveld fit of orthorhombic $Li_{3.34}Mg_{1.33}TeO_6$ to XRD data is shown in Figure 4 and the structural details are given in Table 3. The structure is shown in Figure 5. Finally, we note that no orthorhombic phase of this composition has previously been reported, although an orthorhombic phase has been reported of a Re (for Te) analogue Li_4MgReO_6.[40]
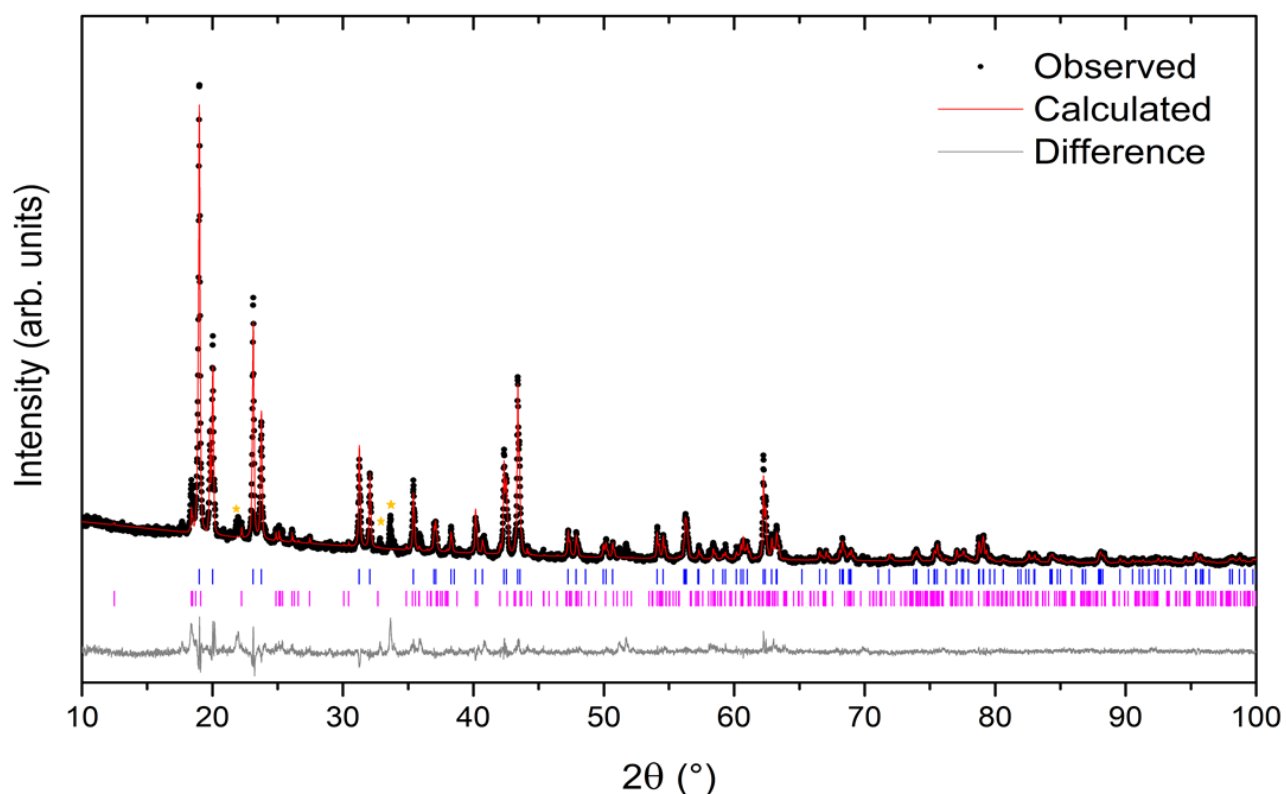

Figure 4: *Rietveld fit of orthorhombic $Li_{3.34}Mg_{1.33}TeO_6$ to XRD data at room temperature from a Cu K_α source (λ= 1.5418 Å). Observed data are given as black circles, calculated fit*

is red and difference curve is grey. Blue tick marks show Bragg reflections for orthorhombic Li$_{3.34}$Mg$_{1.33}$TeO$_6$ and purple tick marks for the impurity Li$_4$TeO$_5$ (~4% weight fraction). The orange stars identify unknown impurity peaks.

Table 3 Unit cell dimensions, fractional atomic coordinates, site occupancies, and isotropic atomic displacement parameters B$_{iso}$ for the orthorhombic phase of Li$_{3.34}$Mg$_{1.33}$TeO$_6$ at room temperature, from Rietveld refinement against XRD data

***Fddd* Li$_{3.34}$Mg$_{1.33}$TeO$_6$** GOF = 2.00, R$_{wp}$ = 9.20%		**Crystal system** Orthorhombic		**Space Group** *Fddd*		
	a (Å)	**b (Å)**	**c (Å)**	**Volume (Å^3)**		
	5.87774(15)	8.5318(2)	17.7239(5)	888.82(4)		
Atom	**x**	**y**	**z**	***Occ.***	***B$_{iso}$***	**Wyckoff Site**
Li$^+$(1)	3/8	3/8	0.0434(5)	0.5	0.20(18)[a]	16*g*
Mg^{+2}(1)	3/8	3/8	0.0434(5)	0.5	0.20(18)[a]	16*g*
Te^{6+}(1)	1/8	1/8	1/8	1	0.24(6)	8*a*
O^{2-}(1)	1/8	0.3499	1/8	1	0.15(13)[b]	16*f*
O^{2-}(2)	0.1076	0.3741	0.2981	1	0.15(13)[b]	32*h*
Li$^+$(2)	3/8	3/8	3/8	0.674(16)	0.20(18)[a]	8*b*
Mg^{2+}(2)	3/8	3/8	3/8	0.326(16)	0.20(18)[a]	8*b*
Li$^+$(3)	3/8	3/8	0.2048(15)	0.837	0.20(18)[a]	16*g*

Table 4: Selected interatomic distances (Å) for orthorhombic Li$_{3.34}$Mg$_{1.33}$TeO$_6$ at room temperature, from Rietveld refinement against XRD data

Te-O1 (x2)	1.922(2)	(Li2,Mg2)–O1 (x2)	2.347(2)
Te-O2 (x4)	1.933(8)	(Li2,Mg2)–O2 (x4)	2.080(4)
Average	1.93	Average	2.17
Sum of radii[38]	1.96	Sum of radii	2.16
BVS (Te^{6+})	5.80	BVS (Li$^+$, Mg^{2+})	0.95, 1.75
(Li1,Mg1)–O1 (x2)	2.073(6)	(Li3)–O1 (x2)	2.05(2)
(Li1,Mg1)–O2 (x2)	2.122(7)	(Li3)–O2 (x2)	2.1432(8)

(Li1,Mg1)–O2 (x2)	2.130(3)	(Li3)–O2 (x2)	2.28(2)
Average	2.11	Average	2.16
Sum of radii	2.14	Sum of radii	2.16
BVS (Li$^+$, Mg^{2+})	1.06, 1.96	BVS (Li$^+$)	0.95

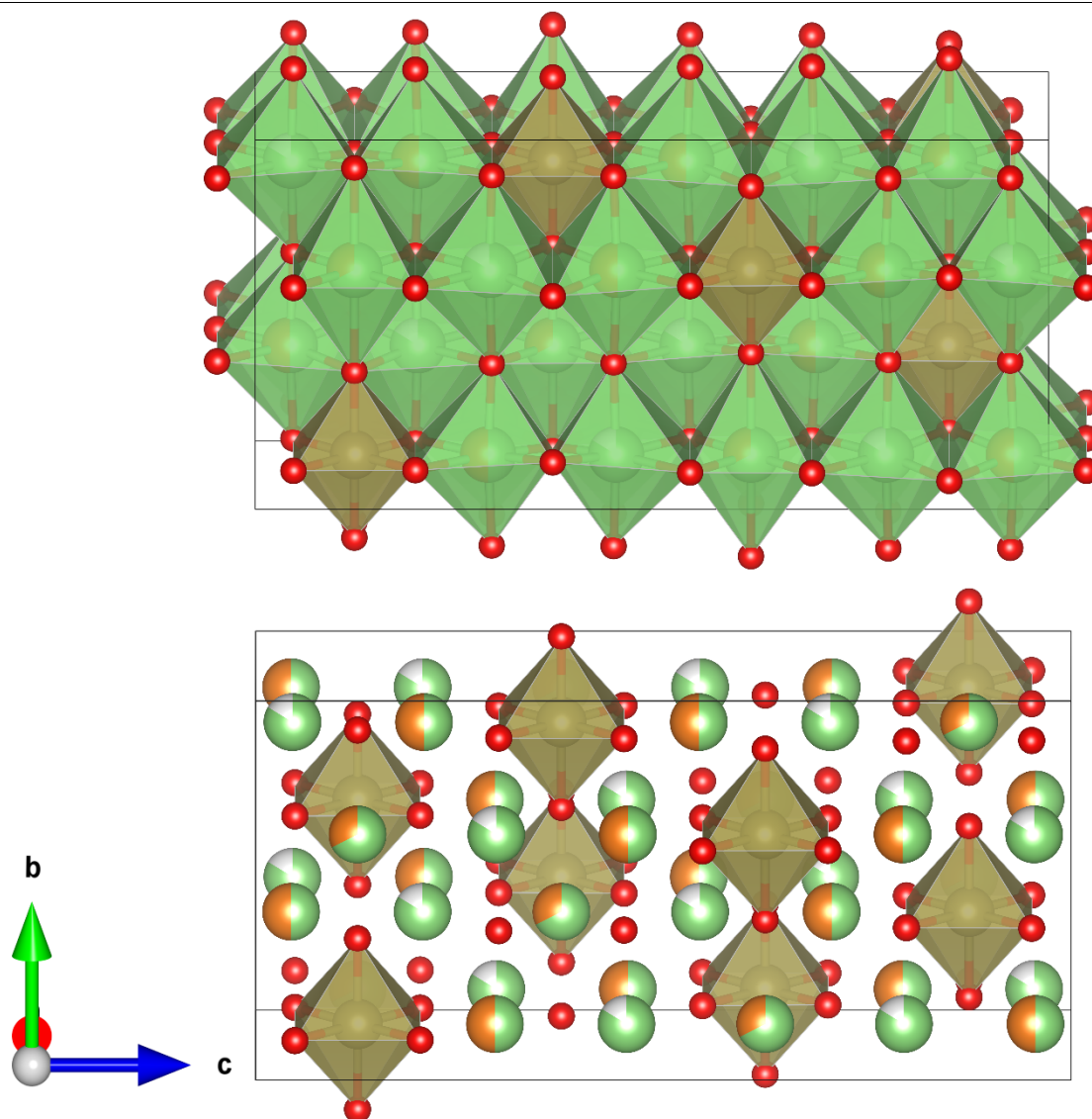**Figure 5:** *Crystal structure of orthorhombic Li$_{3.34}$Mg$_{1.33}$TeO$_6$. TeO$_6$ octahedra are gold, O atoms are red, Li atoms are green. Mg (orange) is distributed across sites which have mixed occupancy with Li, as indicated by wedges.*

Conclusions

When synthesised by solid-state methods, Li$_{4–2x}$Mg$_{1+x}$TeO$_6$ forms two distinct polymorphs depending on the Li:Mg ratio x and the thermal treatment. The monoclinic form at $x \approx 0$

shows strong structural similarity to Li_4ZnTeO_6, the Li_4MTeO_6 (M = transition metal) family and many other "honeycomb" type layered oxides. It shows Li/Mg disorder in the intercalation layers and, similarly to Li_4ZnTeO_6, minor Mg substitution into the Li layer. Slightly Mg-rich compositions $0 < x < {\sim}0.5$ yield a distinct orthorhombic rock-salt type superstructure phase, isostructural to $Li_3Co_2TaO_6$, with ordered TeO_6 octahedra and some anti-site disorder on the Mg and Li sites.

Acknowledgements

References

(1)   Berthelot, R.; Schmidt, W.; Muir, S.; Eilertsen, J.; Etienne, L.; Sleight, A. W.; Subramanian, M. A. *Inorg. Chem.* **2012**, *51* (9), 5377–5385.

(2)   Schmidt, W.; Berthelot, R.; Sleight, A. W.; Subramanian, M. A. *J. Solid State Chem.* **2013**, *201*, 178–185.

(3)   Berthelot, R.; Schmidt, W.; Sleight, A. W.; Subramanian, M. A. *J. Solid State Chem.* **2012**, *196*, 225–231.

(4)   Seibel, E. M.; Roudebush, J. H.; Wu, H.; Huang, Q.; Ali, M. N.; Ji, H.; Cava, R. J. *Inorg. Chem.* **2013**, *52* (23), 13605–13611.

(5)   Viciu, L.; Huang, Q.; Morosan, E.; Zandbergen, H. W.; Greenbaum, N. I.; McQueen, T.; Cava, R. J. *J. Solid State Chem.* **2007**, *180* (3), 1060–1067.

(6)   Greaves, C.; Katib, S. M. A. *Mater. Res. Bull.* **1990**, *25* (9), 1175–1182.

(7)   Wong, C.; Avdeev, M.; Ling, C. D. *J. Solid State Chem.* **2016**, *243*, 18–22.

(8)   Zvereva, E. A.; Evstigneeva, M. A.; Nalbandyan, V. B.; Savelieva, O. A.; Ibragimov, S. A.; Volkova, O. S.; Medvedeva, L. I.; Vasiliev, A. N.; Klingeler, R.; Buechner, B. *Dalton Trans.* **2011**, *41* (2), 572–580.

(9)   Zvereva, E. A.; Nalbandyan, V. B.; Evstigneeva, M. A.; Koo, H.-J.; Whangbo, M.-H.; Ushakov, A. V.; Medvedev, B. S.; Medvedeva, L. I.; Gridina, N. A.; Yalovega, G. E.; Churikov, A. V.; Vasiliev, A. N.; Büchner, B. *J. Solid State Chem.* **2015**, *225*, 89–96.

(10)   Zvereva, E. A.; Stratan, M. I.; Ovchenkov, Y. A.; Nalbandyan, V. B.; Lin, J.-Y.; Vavilova, E. L.; Iakovleva, M. F.; Abdel-Hafiez, M.; Silhanek, A. V.; Chen, X.-J.; Stroppa, A.; Picozzi, S.; Jeschke, H. O.; Valentí, R.; Vasiliev, A. N. *Phys. Rev. B* **2015**, *92* (14), 144401.

(11)   Yuan, D.; Liang, X.; Wu, L.; Cao, Y.; Ai, X.; Feng, J.; Yang, H. *Adv. Mater.* **2014**, *26* (36), 6301–6306.

(12)   Xu, J.; Assoud, A.; Soheilnia, N.; Derakhshan, S.; Cuthbert, H. L.; Greedan, J. E.; Whangbo, M. H.; Kleinke, H. *Inorg. Chem.* **2005**, *44* (14), 5042–5046.

(13)   Kumar, V.; Gupta, A.; Uma, S. *Dalton Trans.* **2013**, *42* (42), 14992–14998.

(14)   Stratan, M. I.; Shukaev, I. L.; Vasilchikova, T. M.; Vasiliev, A. N.; Korshunov, A. N.; Kurbakov, A. I.; Nalbandyan, V. B.; Zvereva, E. A. *New J. Chem.* **2019**, *43* (34), 13545–13553.

(15)   Brown, A. J.; Xia, Q.; Avdeev, M.; Kennedy, B. J.; Ling, C. D. *Inorg. Chem.* **2019**, *58* (20), 13881–13891.

(16)   Kumar, V.; Bhardwaj, N.; Tomar, N.; Thakral, V.; Uma, S. *Inorg. Chem.* **2012**, *51* (20), 10471–10473.

(17)   Grundish, N. S.; Seymour, I. D.; Henkelman, G.; Goodenough, J. B. *Chem. Mater.* **2019**, *31* (22), 9379–9388.

(18)   Evstigneeva, M. A.; Nalbandyan, V. B.; Petrenko, A. A.; Medvedev, B. S.; Kataev, A. A. *Chem. Mater.* **2011**, *23* (5), 1174–1181.

(19)   Nalbandyan, V. B.; Avdeev, M.; Evstigneeva, M. A. *J. Solid State Chem.* **2013**, *199*, 62–65.

(20)   Skakle, J. M. S.; Castellanos R., M. A.; Tovar, S. T.; West, A. R. *J. Solid State Chem.* **1997**, *131* (1), 115–120.

(21)   Gupta, A.; Buddie Mullins, C.; Goodenough, J. B. *J. Power Sources* **2013**, *243*, 817–821.

(22)   Sathiya, M.; Ramesha, K.; Rousse, G.; Foix, D.; Gonbeau, D.; Guruprakash, K.; Prakash, A. S.; Doublet, M. L.; Tarascon, J.-M. *Chem. Commun.* **2013**, *49* (97), 11376–11378.

(23)   Masese, T.; Yoshii, K.; Yamaguchi, Y.; Okumura, T.; Huang, Z.-D.; Kato, M.; Kubota, K.; Furutani, J.; Orikasa, Y.; Senoh, H.; Sakaebe, H.; Shikano, M. *Nat. Commun.* **2018**, *9* (1), 3823.

(24)   Li, Y.; Deng, Z.; Peng, J.; Gu, J.; Chen, E.; Yu, Y.; Wu, J.; Li, X.; Luo, J.; Huang, Y.; Xu, Y.; Gao, Z.; Fang, C.; Zhu, J.; Li, Q.; Han, J.; Huang, Y. *ACS Appl. Mater. Interfaces* **2018**, *10* (18), 15760–15766.

(25)   Li, Y.; Deng, Z.; Peng, J.; Chen, E.; Yu, Y.; Li, X.; Luo, J.; Huang, Y.; Zhu, J.; Fang, C.; Li, Q.; Han, J.; Huang, Y. *Chem. – Eur. J.* **2018**, *24* (5), 1057–1061.

(26)   Deng, Z.; Gu, J.; Li, Y.; Li, S.; Peng, J.; Li, X.; Luo, J.; Huang, Y.; Fang, C.; Li, Q.; Han, J.; Huang, Y.; Zhao, Y. *Electrochimica Acta* **2019**, *298*, 121–126.

(27)   Bera, A. K.; Yusuf, S. M.; Kumar, A.; Ritter, C. *Phys. Rev. B* **2017**, *95* (9), 094424.

(28)   Sankar, R.; Panneer Muthuselvam, I.; Shu, G. J.; Chen, W. T.; Karna, S. K.; Jayavel, R.; Chou, F. C. *CrystEngComm* **2014**, *16* (47), 10791–10796.

(29)   Miura, Y.; Yasui, Y.; Moyoshi, T.; Sato, M.; Kakurai, K. *J. Phys. Soc. Jpn.* **2008**, *77* (10), 104709.

(30)   Coelho, A. A. *J. Appl. Crystallogr.* **2018**, *51* (1), 210–218.

(31)   Avdeev, M.; Hester, J. R. *J. Appl. Crystallogr.* **2018**, *51* (6), 1597–1604.

(32)   Liss, K.-D.; Hunter, B.; Hagen, M.; Noakes, T.; Kennedy, S. *Phys. B Condens. Matter* **2006**, *385–386*, 1010–1012.

(33)   Li, X.; Bianchini, F.; Wind, J.; Vajeeston, P.; Wragg, D.; Fjellvåg, H. *J. Electrochem. Soc.* **2019**, *166* (15), A3830–A3837.

(34)   Politaev, V. V.; Nalbandyan, V. B.; Petrenko, A. A.; Shukaev, I. L.; Volotchaev, V. A.; Medvedev, B. S. *J. Solid State Chem.* **2010**, *183* (3), 684–691.

(35)   Boulineau, A.; Croguennec, L.; Delmas, C.; Weill, F. *Solid State Ion.* **2010**, *180* (40), 1652–1659.

(36)   Bréger, J.; Jiang, M.; Dupré, N.; Meng, Y. S.; Shao-Horn, Y.; Ceder, G.; Grey, C. P. *J. Solid State Chem.* **2005**, *178* (9), 2575–2585.

(37)   Zvereva, E. A.; Savelieva, O. A.; Titov, Y. D.; Evstigneeva, M. A.; Nalbandyan, V. B.; Kao, C. N.; Lin, J.-Y.; Presniakov, I. A.; Sobolev, A. V.; Ibragimov, S. A.; Abdel-Hafiez, M.; Krupskaya, Y.; Jähne, C.; Tan, G.; Klingeler, R.; Büchner, B.; Vasiliev, A. N. *Dalton Trans.* **2013**, *42* (5), 1550–1566.

(38)   Shannon, R. D. *Acta Crystallogr. A* **1976**, *32* (5), 751–767.

(39)   Schulz, H.; Bayer, G. *Acta Crystallogr. B* **1971**, *27* (4), 815–821.

(40)   Milam-Guerrero, J.; Bloed, C. J.; Nguyen, P.-H. T.; Tran, G. T.; Martin, W. P.; Papakostas, D. V.; Toro, J.; Wilson, M. N.; Carlo, J. P.; Luke, G. M.; Melot, B. C.; Gu, J.; Derakhshan, S. *Inorg. Chem.* **2017**, *56* (19), 11633–11639.

(41)   Mather, G. C.; Smith, R. I.; Skakle, J. M. S.; Fletcher, J. G.; R, M. A. C.; Gutierrez, M. P.; West, A. R. *J. Mater. Chem.* **1995**, *5* (8), 1177–1182.

(42)   Heymann, G.; Selb, E.; Kogler, M.; Götsch, T.; Köck, E.-M.; Penner, S.; Tribus, M.; Janka, O. *Dalton Trans.* **2017**, *46* (37), 12663–12674.